

State diagram of polydisperse elastic-disk systems

Wolfgang Vermöhlen

Höchstleistungsrechenzentrum, Forschungszentrum Jülich, D-52425 Jülich, Germany

Nobuyasu Ito

Department of Applied Physics, Faculty of Engineering, The University of Tokyo, Tokyo 113, Japan

(Received 21 November 1994)

Relying on molecular dynamics simulations, we investigate the state diagram of elastic disks in two dimensions in the microcanonical ensemble under the new aspect of different bidispersities and polydispersities, i.e., different particle radii distributions. We find an Alder transition heralded by a plateau in the pressure-density diagram. In terms of dispersity, we see a universal liquid branch. The solid branch and the coexisting region change. The latter vanishes above a critical polydispersity independent of the radius distribution.

PACS number(s): 64.60.Ht, 64.60.Cn, 05.70.Ce, 02.70.Ns

I. INTRODUCTION

The fluid-solid phase transition in repulsive-disk systems [1], now treated for over 30 years by molecular dynamics (MD) and Monte Carlo (MC) simulations, is still a subject of recent interest [2–9]. It is now believed to be a single first-order transition with the coexistence of fluid and solid [2,3,9]. Various purely repulsive particle potentials display the Alder transition, e.g., hard core [2,3,9], r^{-12} [4,5], and Hertzian contact law [8]. The transition is not limited to the atomic scale nor to identical particles. The influence of size polydispersity on the Alder transition was first investigated by Dickinson and Parker [10] in colloidal dispersions. The rather complicated potential forced them to restrict themselves to small systems of 108 particles in three dimensions (3D). They postulated the existence of a critical dispersity beyond which the liquid and the crystalline states merge. More recently, Moriguchi *et al.* [11] have investigated the effect of size polydispersity for colloids interacting via the Yukawa potential, but under nonequilibrium conditions. Using Brownian dynamics they find an additional glass phase and critical polydispersity above which no solid phase exists. For completeness we mention that charge polydispersity also affects colloidal systems [12,13].

Size polydispersity is, besides dissipation and arbitrary shape, one main characteristic of granular media. By investigating polydispersity the knowledge about equilibrium systems will be the base for theoretical understanding of the nonequilibrium situation in granular systems, where dissipation will be included. Our motivation is a better theoretical understanding of this field which will result in explanations of the different phenomena of granular media [14].

Starting with the equilibrium situation we examine the influence of size polydispersity on the Alder transition by investigating different particle-radius distributions. In particular, we consider (i) binary distributions where particles are characterized by two distinct radii and (ii) a continuous distribution allowing a spectrum of sizes. We

use a MD technique with a short-range, repulsive potential (Hertzian contact law), known from granular simulations, especially monodisperse studies [8], and investigate systems in two dimensions with a length between 20 and 135 particle diameters.

Confirming Dickinson and Parker we find that there is a critical degree of polydispersity above which the Alder transition is destroyed and there is no more plateau in the state diagram. However, based on our Fourier analysis, there is still an ordered and a disordered phase above the critical polydispersity.

After a detailed description of the model and the simulation technique in Sec. II we define thermodynamic quantities in Sec. III and present our results in Sec. IV where we add a theoretical approach intended to explain the influence of polydispersity on the state diagram. Section V summarizes the paper.

II. MODEL

A. Particle potential

Let r_i represent the radius of particle i . The potential energy between particles i, j is calculated by the Hertzian contact law [15]

$$V_{ij} = \frac{2}{5} K_N [(r_i + r_j) - |\vec{x}_i - \vec{x}_j|]^{\frac{5}{2}} \times \theta((r_i + r_j) - |\vec{x}_i - \vec{x}_j|), \quad (1)$$

where \vec{x}_i, \vec{x}_j denote the center of masses of the two particles, $\theta(x)$ is the Heaviside function, and K_N is the elastic modulus, which depends on the Young modulus of the material and the radius of curvature of the particle surfaces. Figure 1 illustrates the collision of two particles.

B. Particle radius distribution

We now present the different normalized distributions for particle radii that are used in polydisperse simula-

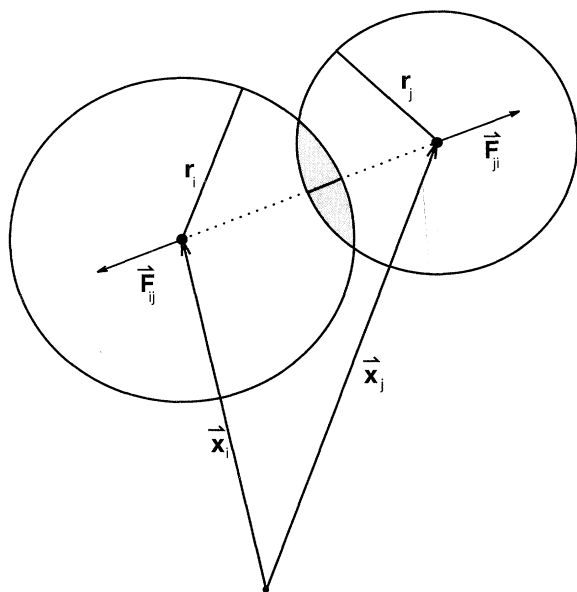


FIG. 1. Elastic-particle collision scheme. Particle i and j experience a repulsive force $\vec{F}_{ij} = -\frac{\partial V_{ij}}{\partial \vec{x}_i}$ if they are touching each other. The force acts along the connection line of the two center of masses and is a function of the overlap length $(r_i + r_j - |\vec{x}_i - \vec{x}_j|)$.

tions [10,11]. We give the relation between their internal parameters and their standard deviation in order to have a criterion to compare these distributions within the context of our simulation and results reported in the literature. In our simulations, we used the binary and the uniform distribution. Figure 2 shows all distributions used together, employing an identical variance.

Gaussian distribution

The most general distribution is the Gaussian distribution that was applied to colloidal systems by Moriguchi

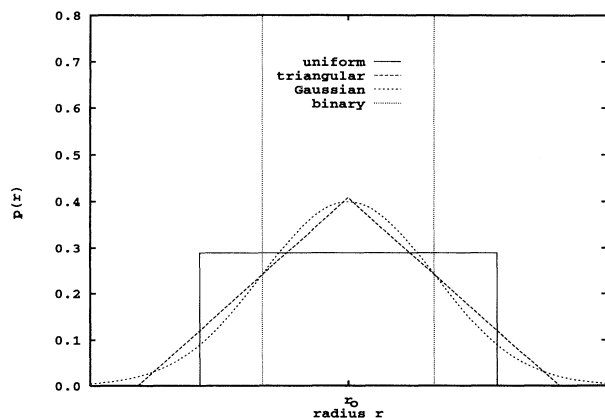


FIG. 2. Different distributions for particle radii with the same variance: uniform, triangular, Gaussian, binary [Eqs. (2)–(5)]. The distribution parameters are given in Table I.

et al. [11]

$$p_g(r) = \frac{1}{\sqrt{2\pi}\sigma} \exp\left(-\frac{(r-r_0)^2}{2\sigma^2}\right). \quad (2)$$

Here, r_0 denotes the mean radius and σ the standard deviation. On a computer the distribution is normally set equal to zero outside a range of $3\sigma - 5\sigma$ around r_0 . As a reference we define a relative standard deviation as $\delta r_g = \sigma/r_0$. The variance is $\text{Var}[p_g(r)] = \sigma^2 = (\delta r_g r_0)^2$.

Triangular distribution

This distribution was used by Dickinson and Parker for modeling the size distribution of colloids [10]. With the triangular distribution one can approximate the Gaussian distribution quite well (see Fig. 2). The distribution can be written as

$$p_t(r) = \frac{\delta r_t r_0 - |r - r_0|}{(\delta r_t r_0)^2} \Theta(r - (r_0 - \delta r_t r_0)) \times \Theta((r_0 + \delta r_t r_0) - r). \quad (3)$$

Here, $2 \times \delta r_t$ denotes the width of the distribution relative to the mean radius r_0 and $\Theta(x)$ is the Heaviside function. The variance of the triangular distribution is $\text{Var}[p_t(r)] = \frac{1}{6}(\delta r_t r_0)^2$.

Uniform distribution

Normal random number generators give a uniform distribution:

$$p_u(r) = \frac{1}{2 \delta r_u r_0} \Theta(r - (r_0 - \delta r_u r_0)) \times \Theta((r_0 + \delta r_u r_0) - r). \quad (4)$$

Again, $2 \times \delta r_u$ gives the width of the distribution relative to the mean radius. The variance of the uniform distribution is $\text{Var}[p_u(r)] = \frac{1}{3}(\delta r_u r_0)^2$.

Binary distribution

This distribution has only two different radii equally weighted:

$$p_b(r) = \frac{1}{2} \left[\delta\left(r - \frac{1}{2}\delta r_b r_0\right) + \delta\left(r + \frac{1}{2}\delta r_b r_0\right) \right]. \quad (5)$$

Here $\delta(x)$ is the Dirac δ function and δr_b is the difference of the two radii of this distribution relative to the mean radius. In this case the variance is $\text{Var}[p_b(r)] = \frac{1}{4}(\delta r_b r_0)^2$.

Table I gives information about how to choose the different distribution parameters in order to get the same variance in reference to the Gaussian distribution. In the following we refer to the binary distribution parameter δr_b as a *bidispersity* and to the uniform distribution parameter δr_u as a *polydispersity*. In this simulation the binary distribution allows the largest degree of polydis-

TABLE I. Different radius distribution. How to choose their parameter compared to the Gaussian distribution parameter to get the same variance.

Distribution	Uniform δr_u	Binary δr_b	Triangle δr_t
parameter	$\sqrt{3}\delta r_g$	$2\delta r_g$	$\sqrt{6}\delta r_g$

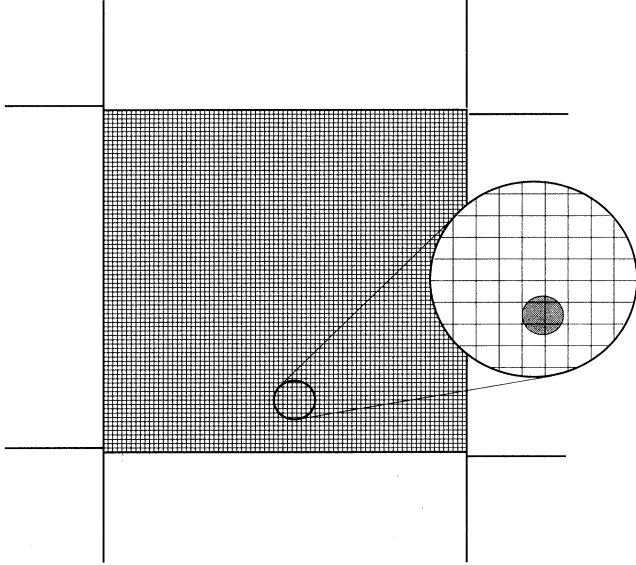


FIG. 3. Division of space in 2D with helical boundary conditions (here, system $L45$, 79×79 cells). The whole volume is sheared a little. This effect vanishes for increasing system size. Zoom: the particle size is chosen so that only one particle can be in one cell in order to apply a fast vectorizable algorithm for the integration of Newton's equation of motion.

persity within a limited radius region for the four different distributions.

Dickinson and Parker proposed a critical polydispersity in their colloidal systems for triangular radius distributions in three dimensions of $\delta r_t^{c3D} = 0.20$ [10] that results, according to [16], in a two dimensions in $\delta r_t^c = 0.34$, which is analog to $\delta r_u^c = 0.24$, $\delta r_b^c = 0.28$, and $\delta r_g^c = 0.14$.

C. Simulation

We simulated the elastic disks in a two-dimensional box of area A with helical boundary conditions as schematically shown in Fig. 3. To integrate Newton's equation of motion we used a standard molecular dynamics technique, namely the Gear predictor-corrector method of fifth order [18]. Our algorithm for a short-range interaction [17] uses an underlying lattice that constrains the particle radii to a certain range (see Fig. 3). We are able to go up to a bidispersity of $\delta r_b^{\max} = 34.31\% \hat{=} \delta r_g^{\max} = 17.16\%$ and a polydispersity in the uniform distribution case of $\delta r_u^{\max} = 17.16\% \hat{=} \delta r_g^{\max} = 9.91\%$ for the zero overlap limit case. For uniform and especially binary distribution the variance is rather large if one considers a finite range of particle radii, as it is necessary in our algorithm. Due to elasticity we also have to take an overlap security range of at least 2% into account. More details of this fully vectorizable algorithm are given in Ref. [17]. The particles were initially arranged on a quadratic lattice and the velocities were chosen randomly to maintain a certain mean kinetic energy. For fast and precise simulations we optimized our model and integration parameter by a time reversal integration test by asking for energy and momentum conservation and reversibility in the phase space for each particle (more details are given in Ref. [8]). The parameters we finally used for the production runs after that optimization procedure are given in Table II.

TABLE II. Simulation parameters for the particle model and the integration algorithm.

Model	$K_N = \frac{1}{\sqrt{2}r_0} 10^6$	elastic modulus
	$r_0 = 0.87777$	particle mass defining the density
	$N = 400$ to $18\,225$	particle number
	$A/(2r_0)^2 = 20 \times 20$ to 135×135	system area
	$\langle \frac{E_{kin}}{N} \rangle = 12.8$	mean kinetic energy per particle
	$f_{corr} = 0.980$	radius correction factor (extrapolation from elastic to hardcore particles)
Integration	$a = 1.0$	cell size $\rightarrow \frac{1}{\sqrt{2}} \leq r \leq 1.0$
	$\Delta t = 5 \times 10^{-4}$	time step

III. THERMODYNAMIC QUANTITIES

During time integration the initial configuration follows a transient before equilibrium is reached. That is, e.g., indicated by the autocorrelation time in the energy and the pressure. In equilibrium we can measure physical quantities. For our systems the transient length was up to 5×10^6 integration steps, that is 100 s simulated time. After that the sampling of the values of interest was done over at least 100 s. To improve the statistics we made runs with different initial configurations determining the mean value of these independent runs. For the data presented we have done about 50 independent runs for one isobidisperse curve in the state diagram and about 130 for the isopolydisperse curves.

We measure the pressure by sampling every 500 time steps 10 times the radial distribution function (RDF) $g(r)$ after the equilibration. $g(r) dr$ is the probability where we find a particle at a distance between r and $r + dr$ from a given particle.

For two-dimensional isotropic fluids one can derive the pressure, P ,

$$\frac{PA}{k_B T N} = 1 - \frac{\pi N}{2A k_B T} \int_0^\infty r^2 g(r) \frac{dV(r)}{dr} dr, \quad (6)$$

in a thermal equilibrium state [19]. P is the pressure, A is the area the particles are allowed to move in, N is the particle number, and $V(r)$ is the elastic potential from Eq. (1). $k_B T$ is the temperature measured according to the equipartition theorem in units of the Boltzmann constant k_B for two dimensions: $\overline{E_{kin}} = \frac{1}{N} \sum_i \frac{1}{2} m_i (v_{x_i}^2 + v_{y_i}^2) = 2 \frac{1}{2} k_B T$. Equivalent to the partition function, the RDF contains the entire information about the fluid.

Systems made of nonattractive particles like the present system [Eq. (1)] have a finite pressure even in the solid phase. Nonzero pressure is necessary to maintain the system at a specific density.

In order to compare the literature with hard-core results we employ the following reduced and hard-core corrected quantities. We introduce a reduced pressure as

$$p_{red} = \frac{PA_0}{k_B T N} \quad (7)$$

with

$$A_0 = \begin{cases} N(2r_0)^2, & \text{for the monodisperse case} \\ \sum_{i=1}^N (2r_i)^2, & \text{for the polydisperse case} \end{cases} \quad (8)$$

and the dimensionless density

$$\rho^* = \frac{A_0}{A}. \quad (9)$$

In monodisperse systems we have for a hexagonal close packing, hcp, $\rho_{hcp}^* = \sqrt{4/3}$, and in the case of a quadratic packing, $\rho_{qp}^* = 1$. Close packing for elastic particles means that nearest neighbors have a distance of their diameter σ .

For theoretical reasons (see Sec. IV C) we also mention an unphysical situation, where the whole system would be occupied by the particles, which is impossible for disks ($\rho^* \leq \rho_{hcp}^*$). This is the situation of packing fraction unity, $\rho^* = 4/\pi$. We call this density the *ultimate density*.

In contrast to the hard-core potential, Hertzian particles have an overlap during collision. This results in an effective radius, smaller than the particle radius r_i . Extrapolation to hard-core behavior can be done by calculating an effective radius due to temperature and elastic potential [8], see Table II. Pressure and density are hard-core extrapolated by a correction factor

$$p_{corr} = p_{red} f_{corr}^2, \quad (10)$$

$$\rho_{corr}^* = \rho^* f_{corr}^2. \quad (11)$$

All simulational data are presented in the corrected version.

Geometrical order as in a local hexagonal structure and/or neighborhood can easily be seen in Fourier space. If we view our particles as pointlike objects, the particle k is represented by

$$f_k(\vec{x}) = \delta(|\vec{x} - \vec{x}_k|) \quad (12)$$

with \vec{x}_k denoting the center of mass position and $\delta(x)$ the Dirac δ function. The total distribution function is

$$f(\vec{x}) = \sum_k f_k(\vec{x}_k). \quad (13)$$

The Fourier transformation reduces to a summation,

$$F(\vec{q}) = \int f(\vec{x}) e^{-2\pi i(\vec{q} \cdot \vec{x})} d\vec{x} = \sum_k e^{-2\pi i(\vec{q} \cdot \vec{x}_k)}. \quad (14)$$

If the system is in a solid phase that has crystal character, we will have six Bragg peaks in a Fourier space placed symmetrically on a ring around the origin of the q space at a typical absolute wave vector $|\vec{q}| = 1/a$, where a gives the mean nearest neighbor distance for the crystal.

IV. RESULTS

A. Bidispersity

We made a system size analysis for different $\delta r_b = 0\%, 11\%, 13\%, 15\%$ and system sizes from 20×20 up to 135×135 particles. We denote the different systems by their length given in mean particle diameters σ_0 . E.g., $L45$ is a system of size $(45\sigma_0)^2$. Results are presented as a state diagram in Fig. 4.

The liquid branch does not change for different system sizes. The solid branch moves towards lower pressure for larger systems, but converges at $\delta r_b = 13\%$ for systems larger than system $L45$. The plateau region shows complicated behavior. For $\delta r_b = 0\%$ the size of the system has nearly no effect. At $\delta r_b = 11\%$ the plateau pressure is still unaffected, but for $\delta r_b = 13\% - 15\%$ we see a non-monotonic change in the plateau pressure with in-

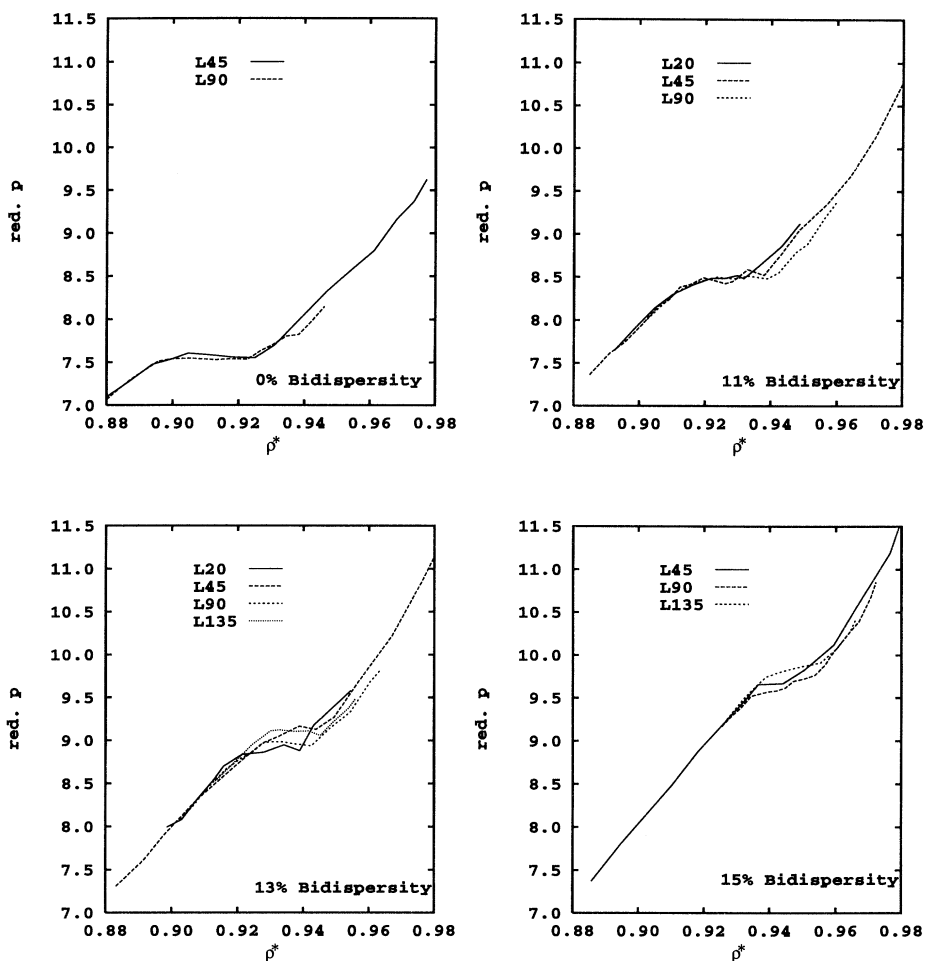


FIG. 4. Reduced pressure over density ($PA_0/k_B T N, \rho^*$) for different system sizes and bidispersities: $\delta r_b = 0\%$, 11%, 13%, 15%; system size: $L20, L45, L90$, and $L135$.

creasing system size. System $L135$ gives an upper limit and system $L90$ the lower limit, while system $L45$ is in the middle of the two larger systems.

The plateau shape gets much clearer for increasing system size because the statistics get better with increasing particle number. There is no clear system size effect that makes scaling possible. Further investigations were done with the system $L45$, which is supposed to have a reasonable ratio of quality to computer time. From the above analysis we expect no qualitative change and only a small quantitative change in the results for larger systems.

For the full state diagram we have done a bidisperse simulation for $\delta r_b = 0\% - 30\%$ at densities between $\rho_{corr}^* = 0.845 - 0.961$ (system $L45$). Figure 5 gives the isobidisperse lines in the state diagram. For $\delta r_b = 0\%$ we get a clear Alder plateau as a coexisting zone separating the fluid branch at lower densities and the solid branch at higher densities. Increasing bidispersity δr_b moves the plateau to higher pressures and densities along the fluid branch. The coexisting region gets smaller up to a critical bidispersity $\delta r_b^c = (13.5 \pm 0.5)\%$ where we have no longer a plateau nor a horizontal tangent to the pressure density curve. Still, a small kink can be seen.

The solid branch is shifted to higher pressures falling on the extrapolation of the fluid branch for $\delta r_b = 25\%$.

There, no kink is seen within the error bar. For $\delta r_b = 30\%$ and $\rho_{corr}^* > 0.900$, we see a systematically lower pressure than for $\delta r_b = 25\%$. With our algorithm we were not able to go to higher bidispersities in order to clarify this trend.

The behavior looks rather similar to the real gas situation where in a pressure-density diagram the isothermals show exactly the same behavior as the isobidispersities here [see Fig. 5(b)].

We show the pressure-bidispersity dependence in Fig. 6 where we can distinguish three domains that are marked by different gray levels. Note that the x axis is $(\delta r_b)^2$. The liquid branch is universal as the horizontal lines indicate in the lower right domain.

The plateau regions are seen in the middle domain where the isodensity lines meet each other. The end of this domain characterizes the critical bidispersity $\delta r_b^c = (13.5 \pm 0.5)\%$. This is equivalent to a Gaussian polydispersity of $\delta r_g^c = (6.75 \pm 0.25)\%$, much smaller than the proposed critical value $\delta r_g^c = 14\%$ of Dickinson and Parker in colloidal systems (compare with the end of Sec. II B).

In the third upper left domain we see a $(\delta r_b)^2$ dependence of pressure that is predicted by cell theory [20] and was found for colloids as well [10].

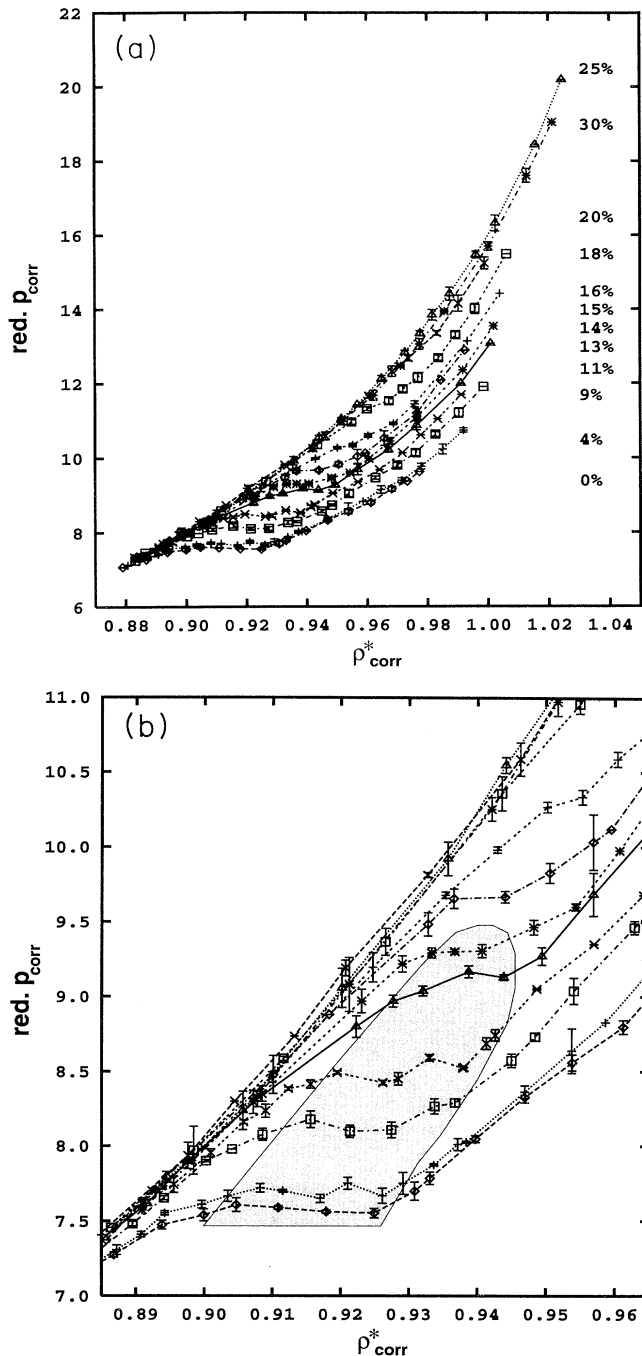


FIG. 5. (a) State diagram: reduced pressure versus density, both hard core corrected for different bidispersities ($\delta r_b = 0\% - 30\%$, system $L45$). (b) Zoom of the plateau region in the state diagram of (a), the gray area points as a guide to the eye to the coexisting region.

B. Polydispersity

For the uniform particle radius distribution we have done runs for polydispersities in the range of $\delta r_u = 0\% - 15\%$. Here we did not go to very high densities but we concentrated on the plateau region $\rho_{corr}^* = 0.845 - 0.922$.

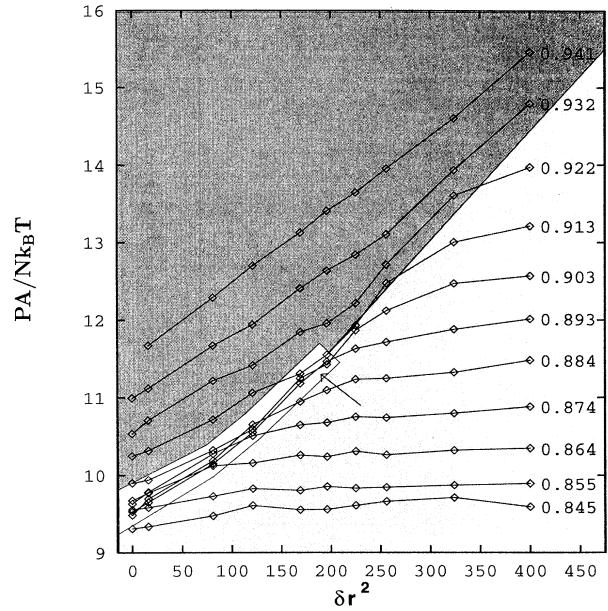


FIG. 6. Pressure over square of bidispersity for different densities: $\rho_{corr}^* = 0.845 - 0.941$. Three different domains can be distinguished and are marked here with different gray levels. We see the universality of the liquid branch as horizontal lines (lower right part) which hold longer for larger polydispersity δr_b . We realize the plateau region where the curves fall on top of each other (middle part) up to a polydispersity of $\delta r_b = 13 - 14\%$ (see arrow). Finally, we see a linear relation between the pressure and the square of the polydispersity for the remaining points which are in the solid branch (upper left part).

Figure 7 shows the isopolydisperse lines in the state diagram for this uniform distribution. Qualitatively they have exactly the same behavior as in the binary distribution case (compare Fig. 5), but here the statistics are much better. Polydispersity δr_u shifts the solid branch and the plateau regions to higher pressures and densities. The coexisting zone vanishes at a critical polydispersity $\delta r_u^c = (11.0 \pm 0.5)\% \hat{=} \delta r_g^c = (6.4 \pm 0.3)\%$. This critical polydispersity has the same value for the binary and the uniform particle radius distribution within the error bar. For higher polydispersities the isopolydisperse lines have an S shape without a horizontal tangent that compares with the kink in the bidisperse system above. At the highest polydispersity, $\delta r_u = 15\%$, solid and fluid branches are no longer distinguishable. There is no transition detectable within the error bar in the state diagram.

The quantitative analysis of the influence of polydispersity on the pressure is given in Fig. 8 [note that the x axis is chosen as $(\delta r_u)^2$]. Compared to the bidisperse situation (Fig. 6) we see a small influence of δr_u on the fluid branch here. The plateaus coincide up to $\delta r_u^c = (11.0 \pm 0.5)\%$. For the solid branch we are lacking more data points for higher densities, so that we are unable to draw any conclusion.

In Fig. 7, the fluid branch for the binary distribution

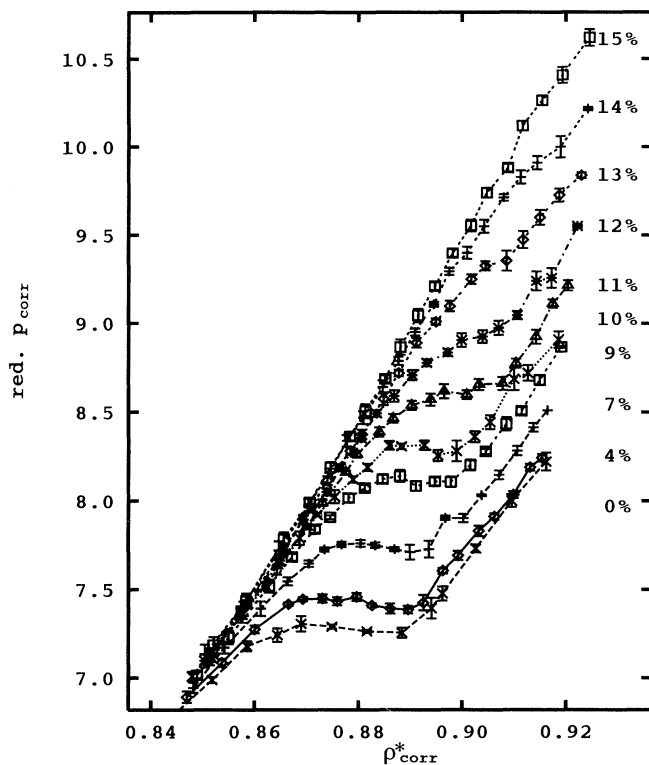


FIG. 7. Isopolydispersity lines in the state diagram for the uniform particle radii distribution ($\delta r_u = 0\% - 15\%$, system L45).

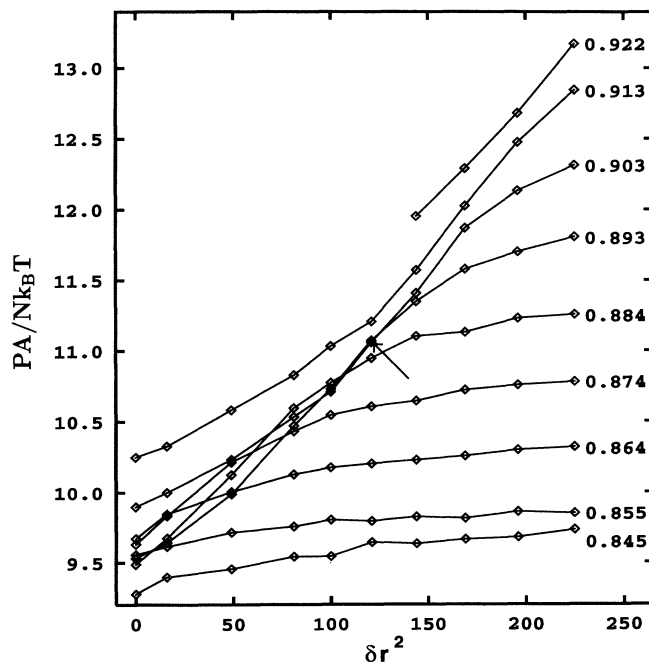


FIG. 8. Pressure over square of polydispersity $(\delta r_u)^2$ for different densities: $\rho_{corr}^* = 0.845 - 0.922$. The parameter range here is not as wide as for the binary distribution. Analog to Fig. 6 the plateau vanishes for $\delta r_u \geq 11\%$ (see arrow).

seems again independent of the polydispersity, but for densities slightly smaller than the plateau region it bends stronger towards the plateau than in the case of the bidisperse system.

We want to characterize the fluid and solid phase by Fourier analysis as described at the end of Sec. III. Figure 9 gives such an analysis for polydispersity $\delta r_u = 10\%$ and 15% , that is below and above $\delta r_u^c = 11\%$, for representative densities (compare with Fig. 7). The peak of order zero for $\vec{q} = \vec{0}$ is not drawn.

For $\delta r_u = 10\%$ we have an Alder plateau in the region of $\rho_{corr}^* = 0.887 - 0.901$ in the state diagram. In Fourier space for $\rho_{corr}^* = 0.845$ we see a clear ring structure giving a characteristic, isotropic length. At the densities $\rho_{corr}^* = 0.895$ and $\rho_{corr}^* = 0.922$ there are six peaks on a ring at a typical length, the latter case having more narrow peaks with smaller bases. We conclude that $\rho_{corr}^* = 0.845$ belongs to the fluid branch (isotropic), $\rho_{corr}^* = 0.895$ is in the coexisting region, where solid peaks exist with a wide basis, and that $\rho_{corr}^* = 0.922$ is the solid phase, more precisely, the ordered phase. This observation coincides with the previous assumptions on the state diagram for $\delta r_u = 10\%$.

For $\delta r_u = 15\%$ the state diagram does not show a fluid-solid transition, respectively, any plateau. But still the phases can be distinguished via Fourier transformation. For $\rho_{corr}^* = 0.845$ and $\rho_{corr}^* = 0.903$ we are in the fluid regime. However for $\rho_{corr}^* = 0.937$ we have a clear peak structure which we identify with the solid or ordered phase.

Polydispersity destroys the Alder plateau, but from the Fourier analysis we conclude that for $\delta r_u = 15\%$ there is solidification without a plateau in the state diagram for high densities.

C. Theory

In this section we draw an idealized scheme of the state diagram for polydisperse systems in 2D to explain our simulational results. The solid branches on the density-pressure plane strongly depend on polydispersity. It has singularity at the close-packing density and the close-packing density is sensitive to different polydispersities. This effects the whole solid branch. We do not know the close-packing density for a given polydispersity of our systems, that is, a system made of nearly hard disks with distributed radii. We obtain some analytical hint for the close-packed density by looking at a *periodic* system of particles of only two different sizes. In Fig. 10 we present the analytical behavior of such an artificial system. For a bidispersity $\delta r_b \leq 30\%$ the close-packed density decreases from $\rho^* = \sqrt{4/3}$ to $\rho^* \approx 1.083$. We assume a similar behavior for an equilibrium packing in our simulation, although the maximum packing is different from the one shown in Fig. 10. In the thermodynamic limit the close-packing density is easily proved to be equal or greater than the hexagonal packing density of the monodisperse system, that is, $\sqrt{4/3}$.

The liquid branches are, however, less sensitive to polydispersity than the solid branch. We do not observe clear

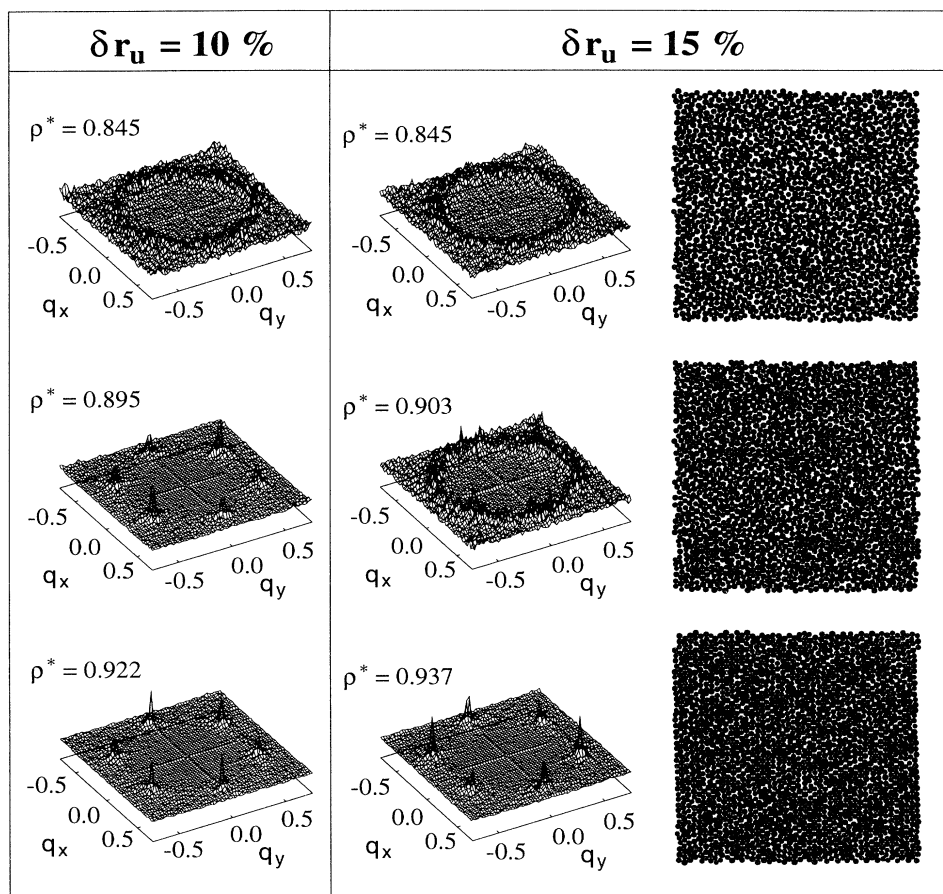


FIG. 9. Fourier analysis of the particle positions for different polydispersity ($\delta r_u = 10\%, 15\%$; system $L45$). For $\delta r = 15\%$ we give the snapshots of the particles as well. The amplitude of the plot containing the ringlike structure is smaller (factor $3/7$) than for the one with the peak structure.

dependencies. So, within the accuracy of our work, we can conclude that polydispersity is irrelevant to the pressure of the liquid state. Assuming that the fluid pressure is the same as in the hard-core system with the same density, we can understand the disappearance of the coexistence plateau between liquid and solid phases when

we increase the polydispersity. The pressure of the hard-core liquid has been studied using perturbation theory and other methods [22–26,21]. It has been observed that its singularity is located at packing fraction unity, that is the ultimate density $\rho_{ultimate}^* = 4/\pi = 1.273$. This is much higher than the hexagonal close-packing density

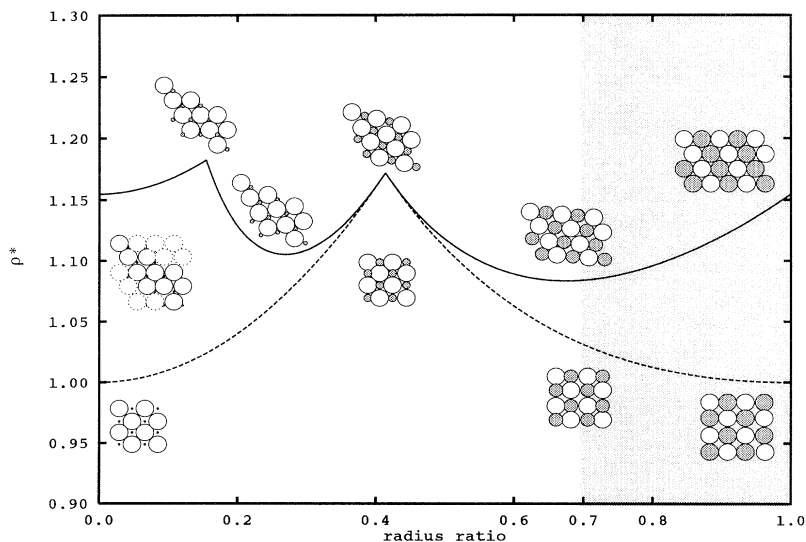


FIG. 10. Influence of bidispersity on periodic, regular dense packing. An infinite system consisting of particles of two different sizes r_{small} and r_{big} with constant particle ratio of $N_{small}/N_{big} = 1$ is considered. If we do not allow demixing and look at the most regular periodic packing, we get the analytical behavior of the close-packing density of a hexagonal (upper curve) and a quadratic (dashed curve) lattice. The smaller particles are gray. Our bidisperse simulations were in the region of $r_{small}/r_{big} = 0.7 - 1.0$. Here, bidispersity reduces the close-packing density ρ^* from $\sqrt{4/3}$ down to 1.083 ($\Delta\rho^* = 0.069$).

$$\rho_{hcp}^* = \sqrt{4/3} = 1.155.$$

At the phase transition the free energy of the solid becomes more favorable than the liquid when the density is increased. At a pressure where the free energy of the solid and the fluid are equal we get a region of coexistence and the change between the two phases is driven by the

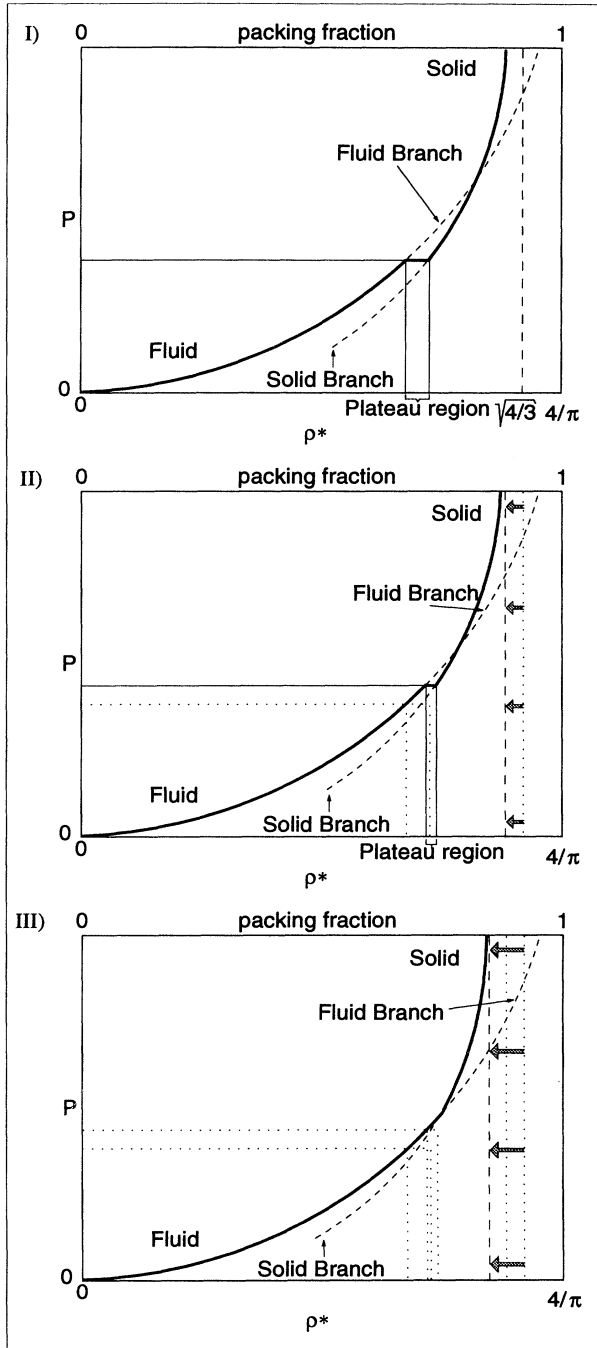


FIG. 11. State diagram for different polydispersity [(I) monodisperse case $\delta r = 0.0$, (II) $\delta r < \delta r^c$, (III) $\delta r > \delta r^c$]. We assume a universal fluid branch diverging at the packing fraction unity, respectively, the ultimate density $\rho^* = 4/\pi$ and a solid branch whose singularity is dependent on close-packing density changed by polydispersity (compare Fig. 10).

density. The mathematical singularity of the liquid is not meaningful because the fluid does not exist at that density. This situation is illustrated in Fig. 11 (I) where the solid line represents the pressure density relation.

The present simulation shows that the polydispersity is favorable to the liquid state. When the polydispersity is increased, the coexistence plateau starts at higher densities. The system then follows the liquid branch to a higher density than that corresponding to the monodisperse transition onset. But for the reasons discussed above the solid branch has its singularity at a lower density than the singular density of the liquid following the above observations for a hard-core liquid. So the plateau is shifted along the fluid branch to a higher density having a decreasing density region of constant pressure, see Fig. 11 (II). Finally, at a critical polydispersity, no plateau will exist, see Fig. 11 (III). The system shows a kink in the pressure-density relation.

For higher polydispersities we can imagine that the transition point where the free energy of the solid is equal to that of the liquid lies at a higher density than the density where the liquid and the solid branches cross. Following this scenario on the vanishing plateau, a jump of pressure may appear for much larger polydispersity than the critical one.

We have not yet observed either the reverse effect or the pressure jump and this may be due to the fact that our simulations are restricted to a degree of bidispersity $\delta r_b \leq 34.31\%$ and a uniform polydispersity of $\delta r_u \leq 17.16\%$. On the other hand, if we follow the argument given in Fig. 10 for bidispersities of $\delta r_b \geq 32\%$, the close-packed density should increase again. Figure 5 has an unsystematic behavior in the solid density region for $\delta r_b = 30\%$. There the pressure is slightly lower than for $\delta r_b = 25\%$. This points to the direction of an again increasing close-packed density, but new simulations in this regime are required to give a precise answer.

V. SUMMARY

We have performed MD simulations with elastic disks obeying the Hertzian contact law in a microcanonical ensemble. We find the Alder phase transition indicated by a plateau in the state diagram. The influence of binary and uniform radius distributions on the transition is investigated.

A systematic system size analysis in the bidisperse system of size $L20$ to $L135$ does not show a clear system size trend. For both radius distributions, we give a state diagram for a large degree of polydispersity [$\delta r_b = (0-30)\%$, $\delta r_u = (0-15)\%$]. The Alder transition is stable up to a critical dispersity parameter $\delta r_g^c = (6.6 \pm 0.3)\%$ for both distributions. The variance of the distributions determines the global behavior of the system independent of the form of the distribution. In comparison with colloidal systems the elastic particles behave more like hard-core particles and so they are much more sensitive to polydispersity and have a smaller δr^c .

By Fourier transformation we characterized the solid and liquid phase and above the critical polydispersity there are still two phases that are distinguishable. The nature of this phase transition is not clear.

With some basic assumptions we outlined a theoretical argument for the understanding of the mechanism behind the behavior of the isopolydispersity lines in the state diagram. The close-packing density and the influence of polydispersity on the close packing were the important points within this argumentation. We explained the existence of the plateau, the vanishing process for an increasing degree of polydispersity, and the kink observed in the simulations above the critical value. All phenomena observed in our simulations are included.

A higher degree of polydispersity is required in the

simulational field to see whether the pressure really goes down again or a pressure gap occurs due to our theory. The observed effects should show up in three dimensions, where polydispersity will have a much stronger effect than in two dimensions.

ACKNOWLEDGMENTS

We would like to thank H. Herrmann for fruitful discussion. The simulations were done on the ZAM Paragon and HLRZ Cray YMP at Forschungszentrum KFA Jülich, Germany, and on the Paragon at Tokyo University, Japan.

-
- [1] A. J. Alder and T. E. Wainwright, *Phys. Rev.* **127**, 2 (1962).
 - [2] J. A. Zollweg and G. V. Chester, *Phys. Rev. B* **46**, 11 186 (1992).
 - [3] J. Lee and K. J. Strandburg, *Phys. Rev. B* **46**, 11 190 (1992).
 - [4] J. A. Zollweg, G. V. Chester, and P. W. Leung, *Phys. Rev. B* **39**, 9518 (1989).
 - [5] J. Q. Broughton, G. H. V. Gilmer, and J. D. Weeks, *J. Chem. Phys.* **75**, 5128 (1981).
 - [6] K. J. Strandburg, *Rev. Mod. Phys.* **60**, 161 (1988).
 - [7] X. Hu and M. Suzuki, *J. Phys. Soc. Jpn.* **62**, 2636 (1993).
 - [8] W. Vermöhlen and N. Ito, *Int. J. Mod. Phys. C* **5**, 1021 (1994).
 - [9] H. Weber and D. Marx, *Europhys. Lett.* (to be published).
 - [10] E. Dickinson and R. Parker, *Chem. Phys. Lett.* **79**, 3 (1981).
 - [11] I. Moriguchi, K. Kawasaki, and T. Kawakatsu, *J. Phys. (France) II* **3**, 1179 (1993).
 - [12] B. V. R. Tata and A. K. Arora, *J. Phys. Condens. Matter* **3**, 7983 (1991).
 - [13] B. V. R. Tata and A. K. Arora, *J. Phys. Condens. Matter* **4**, 7699 (1992).
 - [14] C. Thornton, *Powders & Grains 93* (A.A. Balkema, Rotterdam, 1993).
 - [15] L.D. Landau and E.M. Lifschitz, *Theoretical Physics Volume VII* (Akademie, Berlin, 1989).
 - [16] E. Dickinson and R. Parker, *J. Phys. Lett. (Paris)* **46**, L229 (1985).
 - [17] W. Form (now W. Vermöhlen), N. Ito, and G. A. Kohring, *Int. J. Mod. Phys. C* **4**, 1085 (1993).
 - [18] M. P. Allen and D. J. Tildesley, *Computer Simulations of Liquids* (Clarendon, Oxford, 1987).
 - [19] L. E. Reichl, in *A Modern Course In Statistical Physics*, edited by Edward Arnold (University of Texas Press, Austin, 1980).
 - [20] E. Dickinson, *J. Chem. Soc. Faraday II* **75**, 466 (1979).
 - [21] S. Todo and M. Suzuki, *J. Phys. Soc. Jpn.* **63**, 3552 (1994).
 - [22] J. K. Percus and G. J. Yevick, *Phys. Rev.* **110**, 1 (1958).
 - [23] E. Thiele, *J. Chem. Phys.* **39**, 474 (1963).
 - [24] M. S. Wertheim, *Phys. Rev. Lett.* **10**, 321 (1963).
 - [25] M. S. Wertheim, *J. Math. Phys.* **5**, 643 (1964).
 - [26] M. J. Maeso, J.R. Solana, J. Amoros, and E. Villar, *J. Chem. Phys.* **94**, 551 (1991).

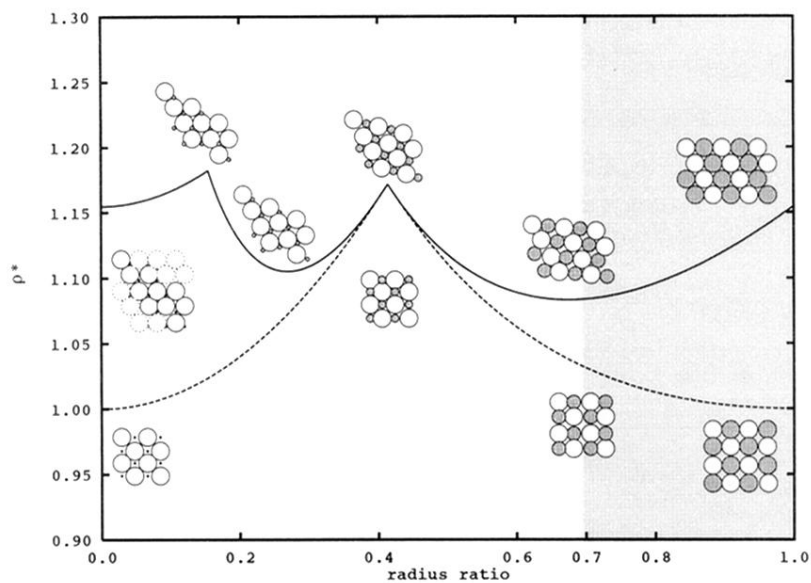


FIG. 10. Influence of bidispersity on periodic, regular dense packing. An infinite system consisting of particles of two different sizes r_{small} and r_{big} with constant particle ratio of $N_{small}/N_{big} = 1$ is considered. If we do not allow demixing and look at the most regular periodic packing, we get the analytical behavior of the close-packing density of a hexagonal (upper curve) and a quadratic (dashed curve) lattice. The smaller particles are gray. Our bidisperse simulations were in the region of $r_{small}/r_{big} = 0.7 - 1.0$. Here, bidispersity reduces the close-packing density ρ^* from $\sqrt{4/3}$ down to 1.083 ($\Delta\rho^* = 0.069$).

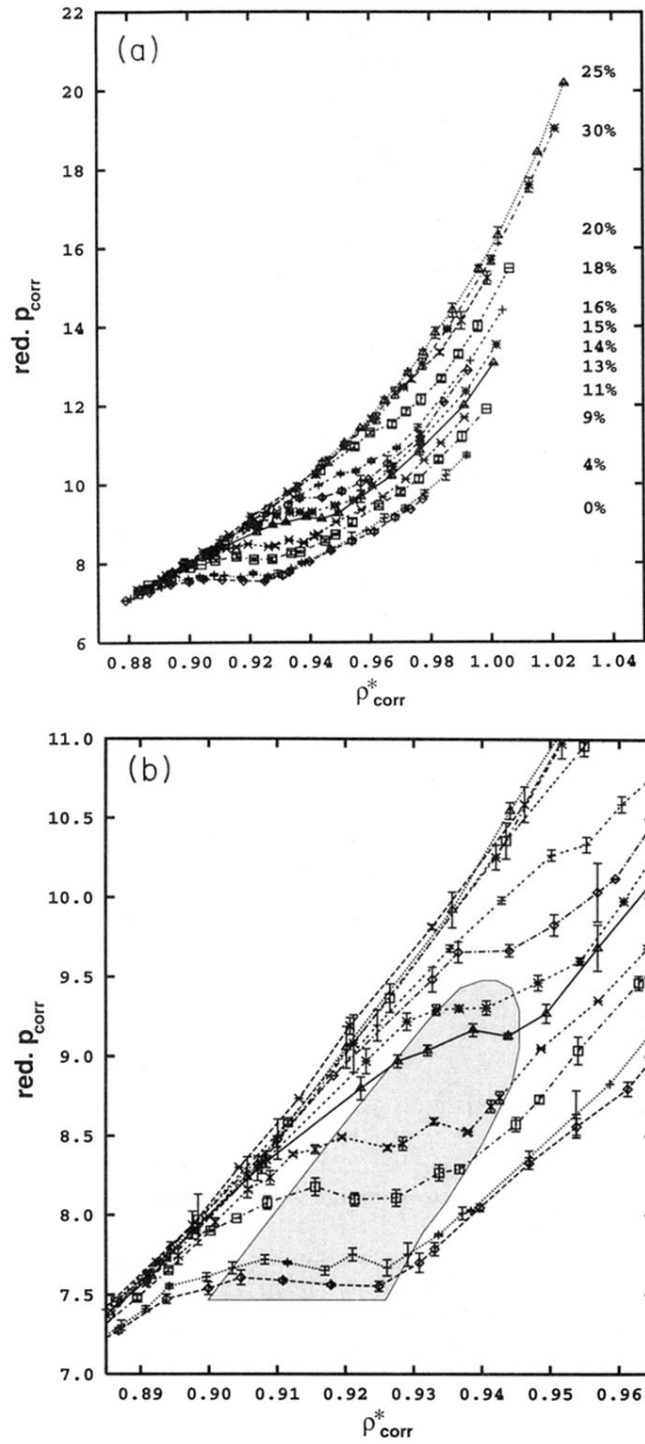


FIG. 5. (a) State diagram: reduced pressure versus density, both hard core corrected for different bidispersities ($\delta r_b = 0\% - 30\%$, system $L45$). (b) Zoom of the plateau region in the state diagram of (a), the gray area points as a guide to the eye to the coexisting region.

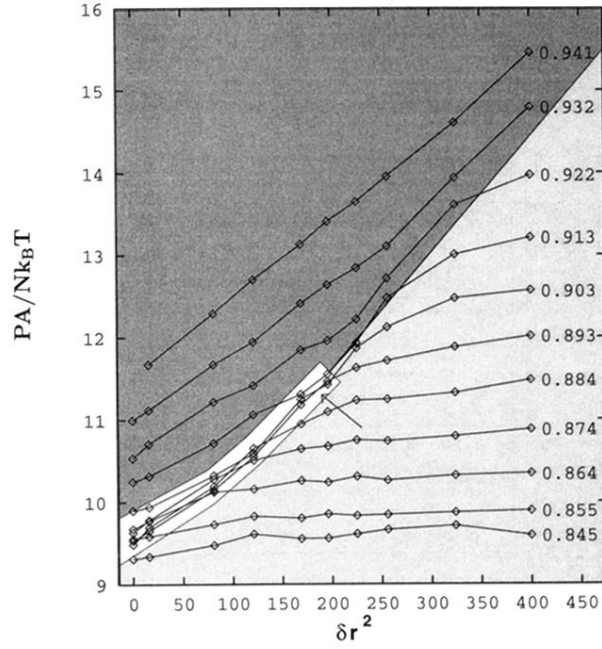


FIG. 6. Pressure over square of bidispersity for different densities: $\rho_{corr}^* = 0.845 - 0.941$. Three different domains can be distinguished and are marked here with different gray levels. We see the universality of the liquid branch as horizontal lines (lower right part) which hold longer for larger polydispersity δr_b . We realize the plateau region where the curves fall on top of each other (middle part) up to a polydispersity of $\delta r_b = 13 - 14\%$ (see arrow). Finally, we see a linear relation between the pressure and the square of the polydispersity for the remaining points which are in the solid branch (upper left part).